



Lateral behaviour of unreinforced masonry walls with different sizes and locations of opening and effect of strengthening measures: a computational approach

Pranoy Debnath¹ · Sekhar Chandra Dutta¹ · Lipika Halder² · Bishwajeet Choubey³

Received: 28 February 2023 / Accepted: 7 October 2023 / Published online: 18 October 2023
© The Author(s), under exclusive licence to Springer Nature B.V. 2023

Abstract

The present paper adopts a sophisticated numerical modeling technique using a plasticity-based simplified micro-model method and the extended finite element method for simulating the nonlinear behaviour of unreinforced masonry (URM) walls with different types of sizes and positions of openings. The validity of this model has been proven by comparing the results subjected to a similar loading obtained by the experimental approach. Thereafter, the validated computational model is used to study the behaviour of the 3D URM wall model with different opening percentages. The effect of the position of the openings is also studied. Further, the load–displacement curves are drawn to provide a clear idea about the load-carrying capacity of the same URM walls. The hysteretic behaviour obtained in each model under cyclic loading gives an idea about the energy dissipation capacity of each of the models studied. The same walls are analyzed by strengthening the walls with two cost-effective materials, wire mesh and polypropylene bands. Since the study on lateral behaviour of masonry walls, particularly regarding the effect of area and the position of the opening, is very rarely available, the present detailed study is believed to be helpful in reducing the seismic vulnerability of actual masonry structures, which always have openings with different sizes and positions.

Keywords Finite-element method · Unreinforced masonry · Openings · Strengthening · Hysteretic behaviour · Cyclic load · Concentrated load

1 Introduction

Masonry structures prevail in very large numbers in many developing countries like Indian subcontinent and places in Europe (e.g. Italy) (Schildkamp et al. 2020). The people belonging to low to middle-income groups often fail to afford structures constructed by reinforced concrete and can only afford masonry structures as low-cost alternatives with less technical input. Since unreinforced masonry cannot take tension, its lateral load resistance capacity is lower than the vertical load capacity. i.e., dead load and live load. Hence, the masonry structures have undergone catastrophic failures with considerable loss of properties and lives during earthquakes.

Extended author information available on the last page of the article

On the other hand, the lateral load capacity of the masonry building along a particular direction primarily depends on the in-plane stiffness and strength of masonry walls available in the direction. Following these behavioral mechanics, considerable research efforts have been made to evaluate the in-plane resistance of the URM walls. (Nayak and Dutta 2016a; Deb et al. 2021; Zhang et al. 2022). However, in reality, the in-plane walls are not continuous. Instead, they may have openings in various positions in the form of doors and windows in order to permit the functional requirements. The openings may reduce the strength of the masonry wall as a whole. A similar trend is also observed for the loading in the out-of-plane direction, where the out-of-plane load-carrying capacity reduces due to the openings in the walls (Khattak et al. 2021). But the quantitative estimation about the reduction in strength, particularly due to the effect of the area and the position of the opening, is very tough.

Indeed, the modelling of brick-masonry elements and their interface is itself very challenging and depends on different aspects (e.g., brick pore dimensions, compaction of the mortar, nature of micro-layer of masonry units, etc. Hendry 1998). In a broader sense, there are two basic types of computational methods for masonry structures: macro-modeling and micro-modeling (Lourenço 2002). The macro-modelling techniques use various formulations to provide a continuous macroscopic description of the nonlinear mechanical behaviour of the masonry wall (e.g., phenomenological plasticity (Brasile et al. 2010), damage mechanics (Pegon and Anthoine 1997) and nonlocal damage-plasticity (Toti et al. 2015; D’Altri et al. 2018) etc.). However, the hypothesis of isotropic material is not suitable. Moreover, the inelastic behaviour of the masonry walls is primarily affected by the discontinuities in the displacement behaviour generated at the brick–mortar interfaces (Vasconcelos and Lourenço 2009). So, the interface elements find widespread application in the numerical study of masonry constructions (Gambarotta and Lagomarsino 1997; Lourenço and Rots 1997; Alfano and Sacco 2006; Fouchal et al. 2009; Parrinello et al. 2009), which mainly emphasizes the requirements of using the micro-modelling techniques for the masonry elements. The discrete element model (DEM) further improves the numerical strategies to analyze the mechanical behaviour of URM systems made with particles, blocks, or multiple bodies (Formica et al. 2002; Casolo 2004; Lemos 2007; Smoljanović et al. 2015; Bui et al. 2017; Beatini et al. 2017; Baraldi and Cecchi 2018). But the main problem is that the DEM approach generally does not account for masonry crushing (Bui et al. 2017). Therefore, it is very challenging to describe the accurate nonlinear compressive behaviour of masonry walls. In fact, it is determined by the texture of the masonry elements, the direction of the compressive stress, and the proportions of the bricks and mortar joints sizes (Stefanou et al. 2014). Additionally, the idea of developing an accurate 3D solid model to consider the in-plane and out-of-plane response of masonry elements was also contemplated. So, a detailed 3D micro-model of the numerical analysis of URM structures is used following the previous research (Abdulla et al. 2017; D’Altri et al. 2018). In this modelling approach, brick and mortar layers are specially modelled by using 3D solid Finite Elements (FEs), adding Drucker-Prager (DP) plasticity laws conceived in the framework of non-associated plasticity (Drucker and Prager 1952). This enables the representation of brick and mortar behaviour during crushing or cracking. A Mohr–Coulomb failure surface characterizes the interfaces with tension cut-off. The coupling of contact-based rigid cohesive interfaces with the 3D nonlinear damage of textured units is used to model masonry interfaces. The interface behaviour is governed by the typical surface-based contact behaviour applied in a FE software named Abaqus (Abaqus 2022). This modelling approach is applied to masonry walls with openings also.

Further extending this study, it was checked that the lateral load capacity of the URM wall elements could improve easily by strengthening. Many researchers have checked it experimentally. The in-plane lateral response of the strengthened URM walls with ferrocement, polypropylene (PP) bands (Yardim and Lalaj 2016), and textile reinforcement mortar (Yardim and Lalaj 2016; Ismail and Ingham 2016; Akhoundi et al. 2018; Shabdin et al. 2018; Giaretton et al. 2018) was investigated in a limited experimental scope. In another study, URM walls were strengthened using several types of meshes made of nylon strips, geogrid materials, and plastic cement bags (Chourasia et al. 2019). Fabric-reinforced cementitious materials (FRCM) are another way to reinforce masonry structures (Babaeidarabad et al. 2014; Sagar et al. 2017; Casacci et al. 2019) with the help of ACI 549 code to calculate the shear capacity of FRCM materials (ACI 2013). Rigorous shake-table experiments also tested some other economic reinforcing measures of URM wall panels with Polypropylene (PP) bands, wire meshes, and L-shaped bars (Bhattacharya et al. 2014; Nayak and Dutta 2016a; Banerjee et al. 2019).

In this context, the present study makes an effort to study the reduction in strength of the masonry walls and calculate the actual lateral load-carrying capacity of masonry structures compared to the overestimated one considered very frequently without giving any consideration to strength due to opening and how it regains its strength due to strengthening. The essential components of the modelling approach are illustrated in the next section. Figure 1 describes the analysis steps involved in this paper.

2 Methodology

Several researchers have followed different approaches of modelling to analyze the URM structures (Lourenço 2002; Petracca et al. 2017; D’Altri et al. 2020). The numerical modelling was conducted by the simplified FEM micro-modelling approach, where the mortar and the masonry elements are considered continuum units (See Fig. 2). The surface boundaries between the masonry bricks are applied through the interaction properties which are readily accessible in the software named ABAQUS. A sample of a real URM masonry wall unit is shown in Fig. 2a; a simplified continuous micro-modelling idealization is shown in

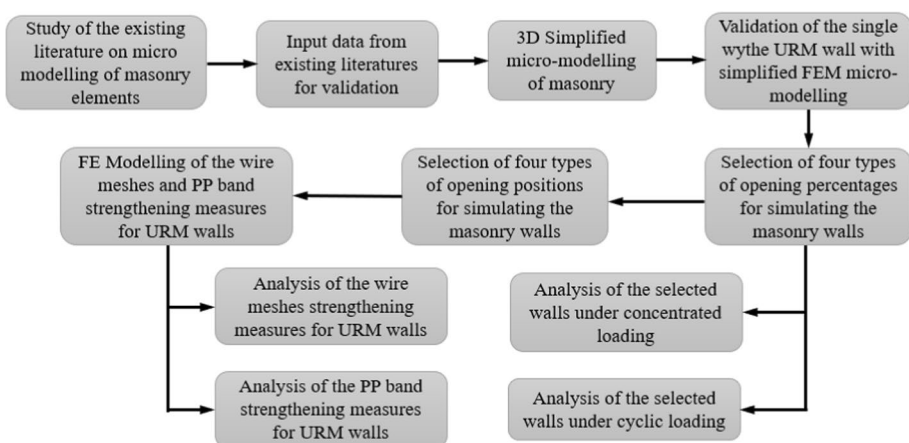


Fig. 1 Analysis steps involved in the paper

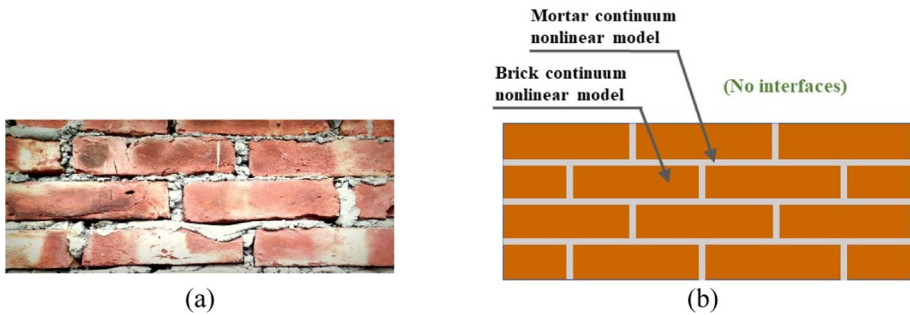


Fig. 2 Modelling strategy for masonry walls **a** masonry wall segment, **b** simplified micro-modelling (following (Lourenço 2002; Petracca et al. 2017))

Fig. 2b. A simplified micro-model has been considered because it takes significantly lesser duration while producing significantly more precise results (Abdulla et al. 2017; Debnath et al. 2023). This method is based on contact penalty formulas and explicit integration methods. The numerical modelling and the material qualities are derived from the previous literature for masonry and mortar units (Lourenço 1996; Abdulla et al. 2017; Debnath et al. 2023). The whole method is explained below in brief.

2.1 Modelling of masonry units

There are mainly five types of failures in the interface between brick and mortar, as described in Fig. 3. Idealization and proper definition of each failure is very important to describe the possible failure modes. The very first one is the failure in pure tensile (see

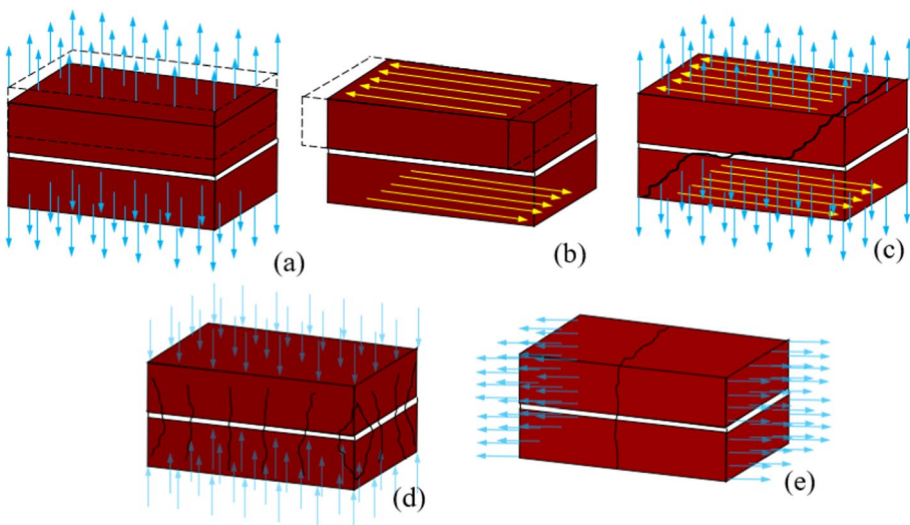


Fig. 3 Typical crack patterns of masonry elements; **a** pure tensile failure of the interface joints, **b** pure sliding shear failure at the interface, **c** diagonal cracking through the assembly, **d** crushing of brick units, and **e** tensile cracking failure of both brick and mortar assembly (described in detail in Lourenço and Rots (1997))

Fig. 3a), then the second one is the failure due to pure sliding shear (see Fig. 3b). Similarly, the third one is the combined failure mode resulting from the cracking and shear failure along the diagonal direction (see Fig. 3c), the fourth one is failure due to the crushing in the masonry unit (see Fig. 3d), and the last one is cracking in the brick units (see Fig. 3e). All the modelling steps for bricks, mortars, and strengthening materials and required equations are described chronologically.

2.1.1 Linear behaviour of the cohesive zone interface joints

The cohesive zone theory for modeling of the interface element was introduced in 1960 by Dugdale (Dugdale 1960) and later developed by Barenblatt (Barenblatt 1962). Basically, the cohesive element can capture the actual results of the interface joints between the masonry units (Bolhassani et al. 2015, 2016; Zhang et al. 2017; Thakur et al. 2020; Salsavilca et al. 2020; Naciri et al. 2021a). In this study, surface-to-surface-based cohesive behaviour is used considering two basic interface failure modes: tensile cracking (Mode-I) and shear sliding (Mode-II–III). The traction–separation law is used here to express the mechanical constitutive model of cohesive behaviour. The surface-based cohesive behaviour can be divided into three stages: the first is linear elastic traction–separation, the second is damage initiation criteria, which correspond to damage occurrence on the interface, and the third is guided by damage evolution rules. Equation (1) defines elastic behaviour by a constitutive matrix that relates the normal and shear stresses to normal and shear damage separations along the interfaces. Here K represents the elastic stiffness matrix, where K_V denotes the normal stiffness and K_{HS} and K_{HT} denote the transverse stiffnesses of the interface elements. The nominal traction stress vector (t) is also consists of three parts: t_V , t_{HS} , and t_{HT} , which basically represent the tractions in normal and two shear directions, respectively. The corresponding separations are denoted by δ_V , δ_{HS} , and δ_{HT} .

$$t = K \times \delta \text{ wheret} = \begin{Bmatrix} t_V \\ t_{HS} \\ t_{HT} \end{Bmatrix}, K = \begin{bmatrix} K_V & 0 & 0 \\ 0 & K_{HS} & 0 \\ 0 & 0 & K_{HT} \end{bmatrix} \text{ and } \delta = \begin{Bmatrix} \delta_V \\ \delta_{HS} \\ \delta_{HT} \end{Bmatrix} \tag{1}$$

The equivalent stiffness (K_V, K_{HS} and K_{HT}) of the interface joints is defined as a function of elasticity modulus of the brick and mortar elements thickness (Lourenço 1996).

2.1.2 Inelastic response of the masonry joints

Initially, the deterioration of the cohesive response at contact surfaces is referred as the initiation of damage. In this criterion, damage occurs when a quadratic interaction function incorporating the contact stress ratios equals one (Campilho et al. 2008). The quadratic stress criterion is utilized in this study to examine the damage initiation criterion at the brick–mortar interface. The equation is expressed in Eq. (2).

$$\left(\frac{t_V}{t_{V,max}}\right)^2 + \left(\frac{t_{HS}}{t_{HS,max}}\right)^2 + \left(\frac{t_{HT}}{t_{HT,max}}\right)^2 = 1 \tag{2}$$

Here t_V denotes the compressive stresses that dominate the fracture behaviour of the masonry joints that is purely excluded from the tension in the normal direction. The

tensile cracking failure of the joints of the masonry assemblage is defined by the shear failure defined by the Mohr–Coulomb failure criteria, as depicted in Eq. (3).

$$\tau_{crit} = C + \mu \times \sigma_n \quad (3)$$

Here τ_{crit} denotes the shear failure criteria of masonry joints, C denotes the cohesion between the surface, μ denotes the coefficient of friction, and σ_n denotes normal compressive stress. Thus τ_{crit} is used to describe shear strength in both directions of the masonry joints ($t_{s,max}$ and $t_{t,max}$). These values may accurately predict the initiation of cracks between the joints and the initial failure modes in sliding shear.

In the post-failure mode definition, the critical shear sliding criteria is defined by $\tau_{sliding}$. The equation is shown in Eq. (4).

$$\tau_{sliding} = \mu \times \sigma_n \quad (4)$$

When the corresponding damage initiation criterion is satisfied, the propagation of the cracks between the masonry joint interfaces causes stiffness degradation at a particular rate and finally reaches the ultimate failure. The damage evolution law is defined based on the linear softening of the fracture energy, which is defined as the area under the traction–separation curve (Abdulla et al. 2017; Debnath et al. 2023). Hence, Eq. (1) can be rewritten as Eq. (5).

$$t = (1 - D) \times [K] \times \{\delta\} \quad (5)$$

Here the damage evolution variable is denoted by D , which gradually increases from 0 to 1 after damage initiation depending on the stresses due to traction. As a result, the linear damage evolution variable is also considered with the dissipation of energy. The corresponding equation is shown in Eq. (6).

$$D = \frac{\delta_{eff,f} \times (\delta_{eff,max} - \delta_{eff,0})}{\delta_{eff,max} \times (\delta_{eff,f} - \delta_{eff,0})} \quad (6)$$

The effective separation is denoted by δ_{eff} , which is defined in Eq. (7) (Camanho and Dávila 2002).

$$\delta_{eff} = \sqrt{\delta_V^2 + \delta_{HS}^2 + \delta_{HT}^2} \quad (7)$$

The effective separation at complete failure is denoted by $\delta_{eff,f}$. The corresponding equation is shown in Eq. (8).

$$\delta_{eff,f} = \frac{2 \times G_{TC}}{t_{eff,0}} \quad (8)$$

Here $\delta_{eff,0}$ defines the separation of the elements at the initial stage of the analysis, $\delta_{eff,f}$ is the actual separation of the masonry elements at ultimate failure load, $\delta_{eff,max}$ defines separation at the ultimate loading condition, $t_{eff,0}$ defines the actual traction at the initiation of damage and G_{TC} defines the mixed-mode fracture energy at the most critical condition, mainly defined by the Benzeggagh–Kenane (BK) fracture criterion (Benzeggagh and Kenane 1996). G_{TC} denotes the critical fracture energy for Benzeggagh–Kenane (BK) fracture law in the mixed mode, as shown in Eq. (9).

$$G_{TC} = G_{IC} + (G_{IIC} - G_{IC}) \times \left\{ \frac{G_{II} + G_{III}}{G_I + G_{II} + G_{III}} \right\}^\eta \tag{9}$$

In the BK law, the exponent value, η , is considered as 2 as masonry joints are considered as brittle material (Benzeggagh and Kenane 1996).

2.1.3 Proposed finite element method for modelling

As a simplified micro modelling approach is adopted for this study, the brick elements are modelled as eight noded 3D hexahedral-shaped units. Hard contact property is used between the adjacent masonry surfaces, i.e., they transfer pressure whenever the surfaces come into contact. The node-to-surface interaction approach is used to establish contact between nearby masonry parts. The extended FEM (XFEM) method can easily execute crack propagation in the masonry units (Belytschko and Black 1999). In XFEM, a new discontinuous function is used in addition to the primary finite-element method (Melenk and Babuška 1996). For simulating the crack pattern, an enrichment function is used by an approximate function of the displacement vector, $\{u\}$ which is independent of the mesh size. The corresponding equation is shown in Eq. (10). In this expression, $N_I(x)$ denotes nodal shape functions, u_I denotes the nodal displacement vector, $H(x)$ denotes discontinuous jump functions primarily signifies the crack pattern, a_I is a vector that denotes the nodal degree of freedom, $F_\alpha(x)$ denotes crack-tip functions and b_I^α denotes the enrichment function of the nodal degree of freedom. This method is employed here through ABAQUS. The expression is shown below (Moes et al. 1999).

$$u = \sum_{I \in N} N_I(x) \times \left[u_I + H(x) \times a_I + \sum_{\alpha=1}^4 F_\alpha(x) \times b_I^\alpha \right] \tag{10}$$

This study also took nonlinear geometrical effects into account. Viscous regularisation and mesh sensitivity analysis is also very important for accurate simulations. An appropriate number of elements should be used to model the masonry elements for accurate converging results. This is practically achieved when a mesh size of $7 \times 2 \times 2$ elements is chosen. After that, the increase in mesh density has an insignificant effect on the results. A detailed analysis is done for different viscosity parameters and different mesh sizes by Abdulla et al. (Abdulla et al. 2017). This study selects 0.002 as the most suitable value for the viscosity parameter. Therefore, the same value is used for this study also.

2.1.4 Drucker–Prager (D–P) plasticity model

The nonlinear property of the masonry brick units can be predicted using the Drucker–Prager plasticity model (Drucker and Prager 1952). Here, the D–P hyperbolic function and non-associative flow rule define the plastic flow potential (Pluijm 1992; Abasi et al. 2020; Naciri et al. 2021b). The expression is shown in Eq. (11).

$$G = \sqrt{(\in \sigma_{i0} \tan \psi)^2 + q^{-2}} - \bar{\rho} \tan \psi \tag{11}$$

Here \in denotes the coefficient representing the eccentricity, σ_{i0} denotes the tensile stress and ψ denotes the dilation angle. This criterion has previously been used to simulate masonry elements such as bricks (Abdulla et al. 2017). The stresses-strains curves are

defined based on the alternate hardening and softening criteria of the D-P plasticity model to obtain the ultimate compressive strength of the FE models. The eccentricity parameter is set at 0.1 by default. In the literature, the dilatation angle for unreinforced masonry structures is commonly assumed to be 36° (Pluijm 1992; Abasi et al. 2020; Naciri et al. 2021b).

2.1.5 Extended elasticity modulus of the masonry units

The extended elasticity modulus is adjusted (E_{adj}) for the expanded masonry units, as the size of the masonry units has to be increased with respect to the actual masonry units. It is mainly determined using a formula that considers the elasticity modulus of the original masonry units and mortar and the geometry of the actual masonry assemblage. Hence, Eq. (12) adopts the uniform distribution of stresses in masonry units considering the even stack bond (Abdulla et al. 2017; Wilding et al. 2020).

$$E_{adj} = \frac{H \times E_u \times E_m}{n \times h_u \times E_m + (n - 1) \times h_m \times E_u} \quad (12)$$

where H denotes the wall height, and n denotes the number of layers. The other parameters are defined in the previous equations. All the selected values are shown in Table 1.

2.2 Numerical modelling of the strengthening materials

Seismic strengthening aims to increase the ultimate strength of a building by strengthening its capacity to absorb inelastic deformation. This can be accomplished by altering the structural system such that energy is transported via alternate load paths or by enhancing the ductility of the constituent parts of the structural system. Some real-life examples are

Table 1 Properties of the constitutive masonry units and the interface joints

Name of properties	Categories	Properties	Values	Units	
Elastic properties	Mortar	E_m	780	MPa	
		ν	0.15		
	Brick units	E_u	16,700	MPa	
		Expanded units	E_{adj}	4050	MPa
	Joint interface stiffness		K_V	82	N/mm ³
			K_{HT}	36	N/mm ³
K_{HS}			36	N/mm ³	
Properties of the joint interfaces nonlinear material	Tension	G_{IC}	0.018	N/mm	
		$t_{V,max}$	0.25	Mpa	
	Cohesion	c	0.350	MPa	
		Shear	G_{IC}	0.125	N/mm
			μ	0.75	
	Compression	σ_c	10.5	MPa	
Properties of the extended masonry elements	Tensile Properties	G_{IC}	0.08	N/mm	
		Tensile strength	2.0	MPa	
	Shear Properties	G_{IC}	0.50	N/mm	
		Shear strength	2.8	MPa	

Fig. 4 Strengthening of the masonry building with PP band in Nepal (Macabuag et al. 2012; Heydariha et al. 2019)



Table 2 Properties of strengthening material used (Nayak and Dutta 2016a; Banerjee et al. 2019)

Type of material	Property	Numerical value
PP band	Width	10 mm
	Density	0.91 g/cm ²
	Thickness	0.85 mm
	Yield strength	12–43 MPa
	Ultimate strength	19.7–80 MPa
Wire mesh	Size of each rectangle in the mesh	3.12 mm X 2.54 mm
	Diameter of the wire	0.12 mm
	Ultimate strength	700 a

shown in Fig. 4 (Macabuag et al. 2012; Heydariha et al. 2019). These structures have been retrofitted in Nepal.

Many methods are available for seismic strengthening of an unreinforced masonry wall, such as ferrocement, post-tensioning, shotcrete, grout and epoxy injection etc. (Babaeidarabad et al. 2014; Yardim and Lalaj 2016; Ismail and Ingham 2016; Sagar et al. 2017; Akhoundi et al. 2018; Shabdin et al. 2018; Giaretton et al. 2018). Each of these methods has many advantages as well as disadvantages. However, sometimes the cost of retrofitting is not reasonable. So, these methods are not suitable for developing countries. Therefore, some cost-effective measures like wire meshes and polypropylene (PP) bands are also tried experimentally for strengthening URM walls (Nayak and Dutta 2016b, a). The same cost-effective strengthening measures are used here for numerical analysis of the strengthened URM walls. The quantitative results will show the effectiveness of the cost-effective strengthening measures in resisting earthquake loadings in a very accurate way. Previously some researchers used the similar method for the numerical modelling of the strengthening materials (Abdulla et al. 2018; Debnath et al. 2023).

ABAQUS software has used a finite element model for modelling and pasting the wire meshes. As done in the experiment, commercially available wire mesh properties are procured from the local market, as used in previous studies (Nayak and Dutta 2016a, b; Banerjee et al. 2019). The same properties are used here for the numerical modelling of the wire meshes. The tensile strength is also considered from the experimental test results, which have been done as wire mesh grids. All considered values for modelling the wire meshes are shown in Table 2. These wire meshes and PP bands are anchored on the walls and pasted with a cement-sand mortar layer with 1:5 ratio. Hence, these elements are considered as a continuum shell element and pasted as a layer for taking stresses as tie constraints. Nonlinear SHELL element is used with six degrees of freedom in each node (Abdulla

et al. 2018). In this study, a perfect bond between the materials is assumed. The cohesive property of the strengthening materials and the URM walls are considered using the tie constraints definition available in ABAQUS. The strengthening materials are considered orthotropic and exhibit lamina behaviour, remaining in an elastic state. The elastic strain values for these materials are assumed to be fixed, as mentioned in (Zhang et al. 2017). For the current analysis, the delamination and fracture failure of the strengthening materials is not considered. The elements are meshed in a manner where each strip is divided into 210 elements. This meshing approach has been previously employed in the literature (Abdulla et al. 2018; Debnath et al. 2023) and has been verified for accuracy through a sample convergence study. The present study examines the in-plane behaviour of URM walls strengthened with wire meshes subjected to lateral loading.

3 Validation

Validation of the accuracy of the proposed model is essential for further simulation. An idealized model of a masonry wall under quasi-static in-plane cyclic loading is validated with the previously done experimental models (Lourenço and Rots 1997; Macorini and Izzuddin 2011; D'Altri et al. 2018).

This wall is considered as a single wythe of brick in the idealized model. The wall is modelled as fourteen (14) courses of bricks. The dimensions of the bricks are 240 mm in length, 120 mm in width and 75 mm in height. The URM wall dimensions for the validation program are denoted 960 mm in length, 120 mm in width and 1050 mm in height. The mortar layer is considered as 10 mm of thickness. The water content is considered according to the Indian standard codes, and the cement-sand ratio is used here as 1:5. All the values are verified from (IS 2250 1981; IS 456 2000; Debnath et al. 2023). Along with this, the mortar layer is also adjusted (E_{adj}) in the simplified micro-model. The interaction properties are assigned between the brick unit surfaces as used for mortar. The top and bottom beams are considered as rigid beams. The adjacent courses of the brick elements are fixed with rigid beams for proper transfer of the applied forces. The beam attached at the bottom of the wall is fixed to the ground. Vertical compressive stress was applied on the top of the beam added on the wall for uniform distribution of stresses. Then the transverse (out-of-plane) movement of the wall was restrained. Finally, a displacement control load was applied horizontally at one side of the top beam, as shown in Fig. 5a. The displacement time history is shown in Fig. 5b.

The results were analyzed using the three distinct displacement values shown in Fig. 6. The displacement values are denoted as point A, at which the first visible crack in the analysis was observed. The ultimate failure in the walls was designated as Point C. Point B denoted the displacement value matching to the maximum load values acquired from numerical simulations. The ultimate failure criterion is considered for this study, as designated by point C.

The numerical simulation result of the proposed model shows a similar agreement with the previous experimental results. A good agreement between the observed crack patterns can also be noted. Figure 7 shows the stress distribution over the whole wall. The cracks were developed in the wall unit, leading to stress redistribution, resulting in the combined diagonal and sliding shear failure due to cyclic loading. Figure 8 represents the experimentally obtained load–displacement diagram for the imposed vertical stress of 0.7 MPa (Mojsilović and Page 2009) compared with the numerical load–displacement diagram

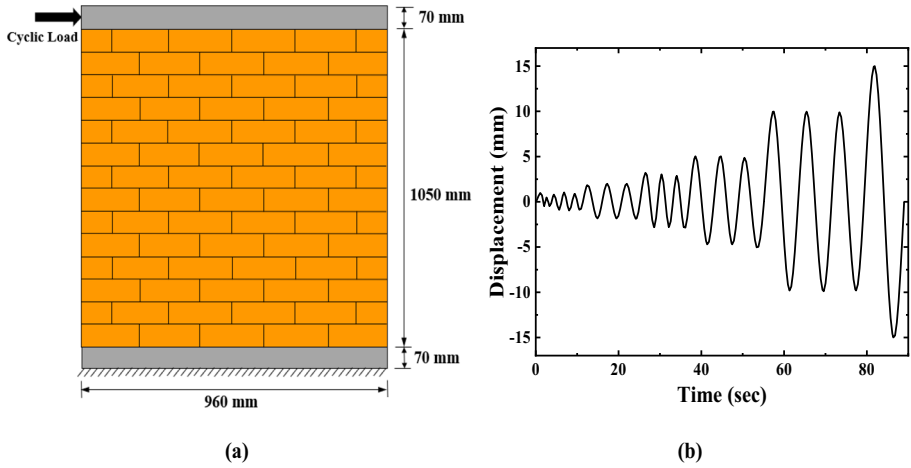


Fig. 5 a Test setup for the masonry assemblage under cyclic loading, b Displacement time history

Fig. 6 Control points of the horizontal load–displacement response

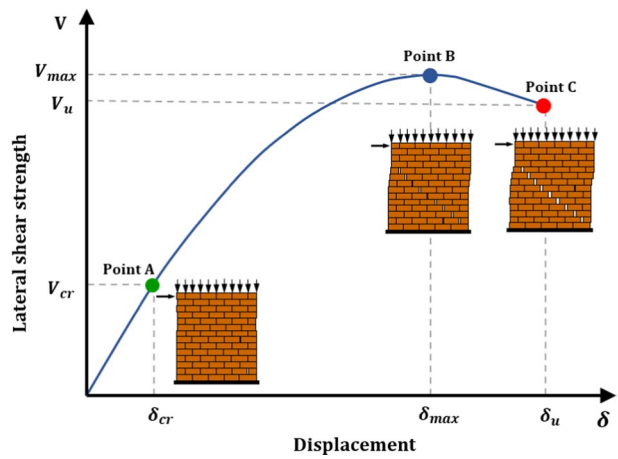


Fig. 7 Failure pattern of the numerical model of the proposed URM wall (Stresses are in N/m²)

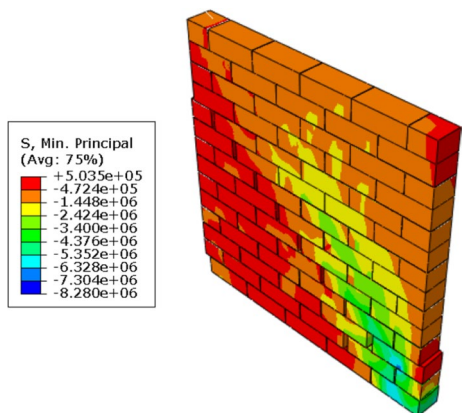
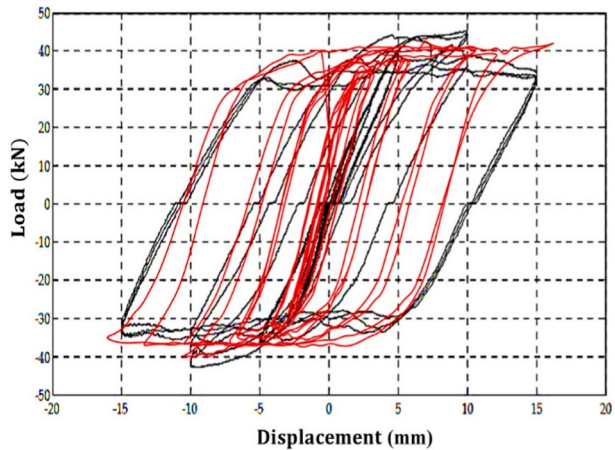


Fig. 8 Comparison between the horizontal load v/s displacement responses for the experimental model (Mojsilović and Page 2009) and the proposed numerical model



of the proposed model, which is quite similar to the experimental results. Some other researchers also validated the same numerical model of the under out-of-plane cyclic loading (D'Altri et al. 2018; Deb et al. 2021).

4 Case studies of the masonry walls with openings

The in-plane performance of the masonry walls is very important for analyzing the URM buildings. Therefore, it is wise to check the performance of the masonry walls with different opening percentages under the above-mentioned lateral in-plane loading. The specimens included masonry walls with four configurations. The first one is without opening, the second one has 25% opening, the third one has 50% opening, and the fourth one has 75% opening. Within the limitation of the single paper, the different types of masonry walls with different openings are shown in Fig. 9. Each of these walls is subjected to concentrated and static cyclic loading at the same place. The first kind of loading will help to understand the load–displacement behaviour of such walls and facilitate the comparison of four types of walls. On the other hand, the repetitive/cyclic loading helps to realize how much hysteretic energy the walls can dissipate and how the presence of opening influences such energy dissipation capacity.

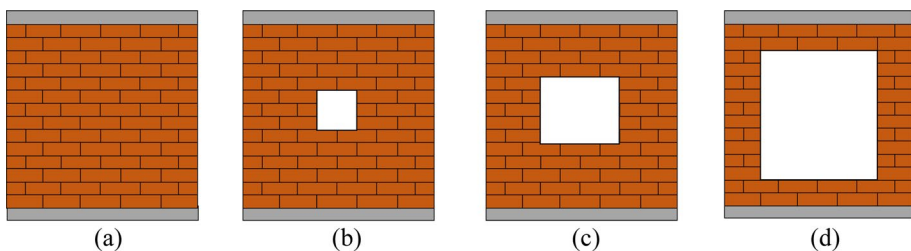


Fig. 9 Masonry wall modelling for in-plane testing of loading, **a** wall with no opening, **b** wall with 25% opening, **c** wall with 50% opening, and **d** wall with 75% opening

4.1 Effect of in-plane concentrated loading

The URM walls were modelled to simulate under in-plane concentrated loading conditions showing different failure patterns, which is really interesting to discuss. Figure 10 shows the min principal stress patterns for the walls with different opening percentages. The load–displacement behaviour of the four walls is shown in Fig. 11. The first wall is not having any openings, while the next walls have 25%, 50%, and 75% openings, respectively. The load–displacement curve for the walls without opening does not exhibit a smooth trend. Further, when the load attains 40 kN, then diagonal shear failure starts, and a drop in load-carrying capacity is observed. Then this process of diagonal shear failure continues up to the ultimate failure of the wall approximately at 45 kN of load and 6 mm of displacement. A similar kind of load–displacement curve was observed in the previous literatures where the masonry walls without opening were modelled in a similar manner (Abdulla et al. 2017; Debnath et al. 2023).

On the other hand, the URM wall with 25% opening throughout exhibits a lesser load-carrying capacity than the previously mentioned case, i.e., the wall without an opening. This is also expected, but the failure pattern is different from the previous case. In this case, the failure initiates from the corners of the openings, and the crack keeps propagating with the increase in load up to the failure. Hence the failure load is 40 kN though the ultimate

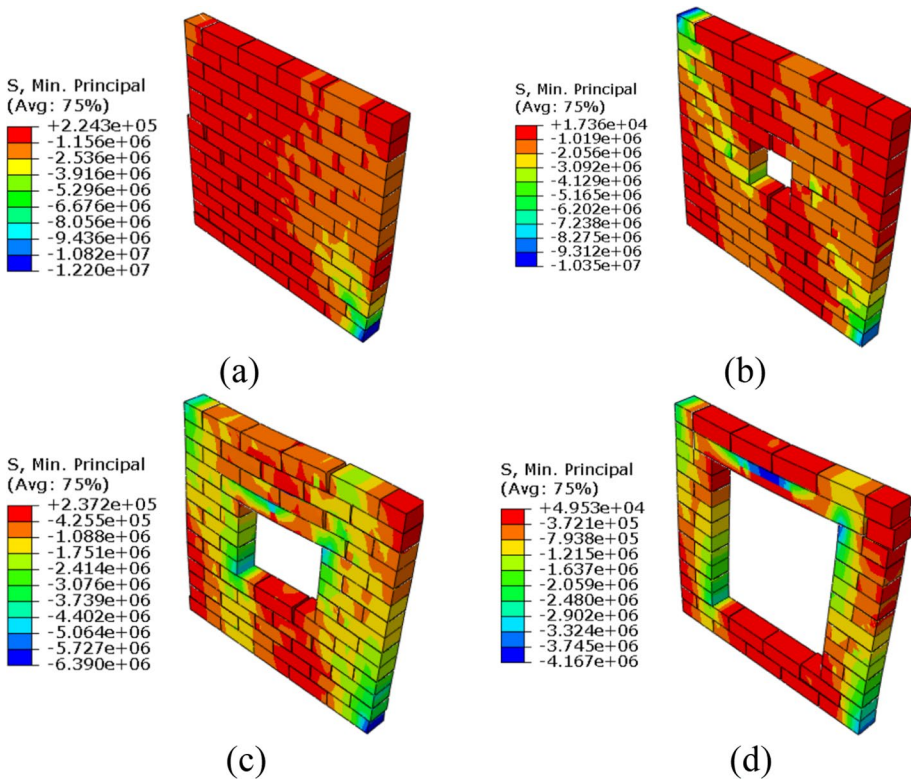
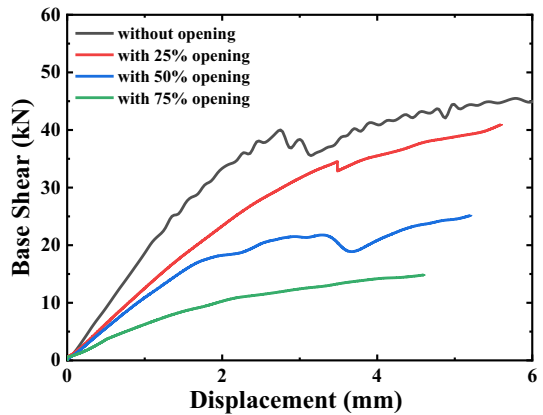


Fig. 10 Min principal stresses diagram (N/m²) of the masonry walls undergoing in-plane concentrated loading, **a** wall with no opening, **b** wall with 25% opening, **c** wall with 50% opening, **d** wall with 75% opening

Fig. 11 Lateral load–displacement diagram undergoing in-plane quasi-static concentrated loading of the URM walls with different opening percentages



displacement is almost the same, i.e., 5.7 mm. Following the same trend, the wall with 50% opening has a lesser load-carrying capacity than the wall with 25% opening. The masonry wall with 50% opening can take up to 24 kN loading, and the maximum displacement is 5.3 mm. A similar trend is observed for 75% opening in the wall when the load–displacement curve shows the lowest load-carrying capacity, indicating the lowest strength, i.e., 14 kN. The ultimate displacement is 4.8 mm. The ultimate displacement in each case is decided by the fact that while crossing this displacement, the wall undergoes collapse, losing all its load-carrying capacity.

4.2 Effect of in-plane cyclic loading

The same series of URM walls with different opening percentages were simulated to investigate the behaviour of the masonry walls when a displacement control-based cyclic loading is applied at the top. Figure 12 shows the min principal stress patterns for the walls with different opening percentages. Figure 13 presents the load–displacement hysteresis behaviour of four walls, as mentioned in the previous section.

Comparing Fig. 12a–d, it may be found that the maximum tensile stress has been developed in the order of 0.9 N/mm^2 because the masonry walls cannot take more tensile stress than that. Hence the tensile stress is generated when the load is applied, and such tension is generated over a much larger region below the area of the diagonal going from the upper corner (where the load is acting) towards the other diagonally opposite corner. So, the failure occurs because of a larger tensile zone and such a wall without opening can take about 45 kN of lateral cyclic loading. As expected, the lateral load-carrying capacity keeps on reducing when the opening starts increasing, as observed in earlier cases. On the other hand, such a vast tensile zone cannot propagate over a larger area, possibly because of the presence of the opening. However, the load-carrying capacity for the wall with 50% opening comes down to 25 kN. For 75% opening, the load-carrying capacity further comes down to 15 kN. Hence, it can be stated that the reduction in strength is almost similar to the reduction in the area of the brick wall due to opening in a very approximate sense.

However, the overall behaviour of the masonry wall is almost similar as observed for the walls with concentrated loading applied in the previous section. The hysteresis curves shown in Fig. 13 imply that the opening reduced the ductility and energy dissipation capacity very sharply with the decrease in the area of the curve. It may be realized

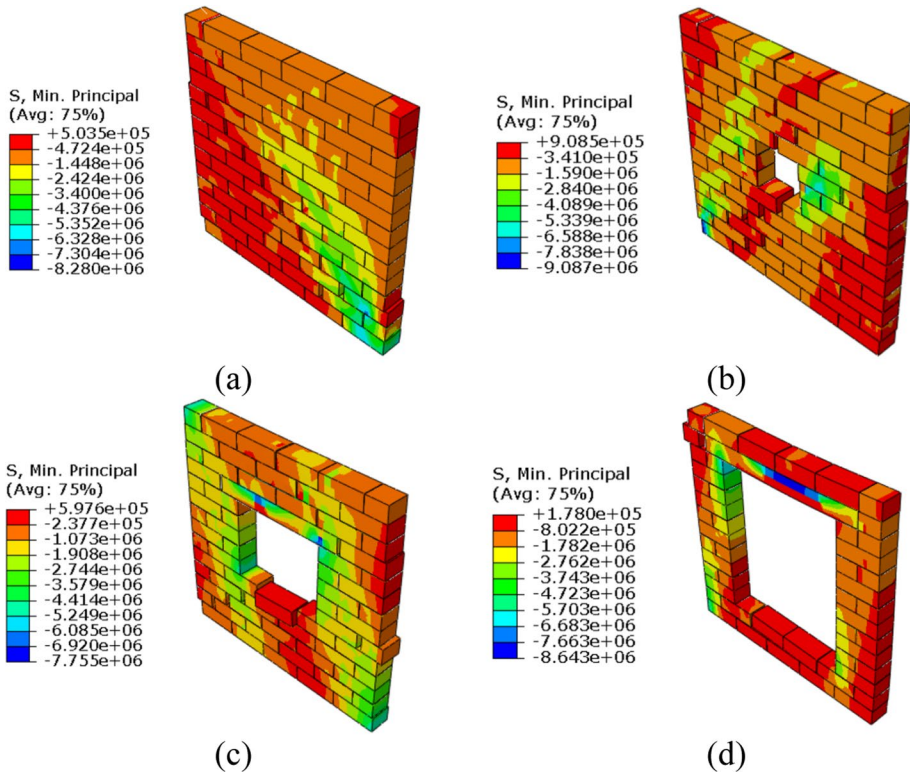
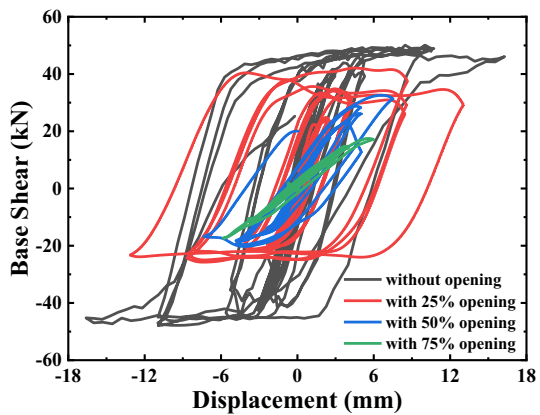


Fig. 12 Min principal stresses diagram (N/m^2) of the masonry walls undergoing in-plane cyclic loading, **a** wall with no opening, **b** wall with 25% opening, **c** wall with 50% opening, **d** wall with 75% opening

Fig. 13 Hysteresis load–displacement diagram of the masonry walls under cyclic loading with different opening percentages



that the wall with 75% opening almost loses ductility as well as energy dissipation capacity. The cases with 50% and 25% openings exhibit ductility and energy dissipation capacity in between the two extreme cases.

For the sake of academic interest, the behaviour of the masonry wall with 25%, 50%, and 75% opening has been studied to develop an insight into the effect of the opening. However, in reality, the opening in most of the cases becomes above 50%. Thus, the quantitative estimation of the reduction in the lateral load-carrying capacity and reduced inelastic deformation due to 50% opening as compared with the wall with no opening may be used as a broad guideline for the design of masonry buildings. It may be physically interpreted that the occurrence of a larger tension zone due to the presence of an opening reduces stress and ductility. Further, the stress concentration at the corners is identified for the formation of such a tensile zone, which implies that the crack is propagating. In fact, because of this reason, when PP band and wire meshes have been added, then they attribute a considerable amount of tension carrying capacity resulting in the tensile zone created due to which stress concentrations is minimized, as elaborated later in Sect. 4.4.

As seen in Figs. 6 and 8, it is seen that the micro-model approach can predict the crack that occurred in various parts of the URM wall with sufficient accuracy. Tensile stress appeared at the mortar joints of the upper and lower side corners of the openings in the early phases of the simulation (Fig. 14). The maximum plastic stresses at Point B revealed that the staircase pattern of failure began at the lower corner of the opening and progressed through mortar joints. The diagonal failure line moved from the upper corner of the opening towards the top portion of the wall at Point C, generating a cracking pattern looking like that of stepped nature (10–15 mm), which became more visible around the opening.

4.3 Influence of the presence of an opening at one side or corner of the wall

In this subsection, the distribution of principal stress, hysteretic energy, and the curve exhibiting hysteretic behaviour are presented for each of the cases studied. As may be understood from the heading of the subsections, the openings are placed at the various openings peripheral as well as corner positions to see the effect of location change and also to examine whether the vulnerability increases due to such irregular placement of openings as compared to the wall in which the openings are placed at the central positions. The wall without an opening and with an opening at the centre are studied to see the variation of stress distribution and hysteretic energy dissipation. These two cases are presented as a reference and the corresponding stress distribution and hysteretic behaviour curve. Three cases for irregular openings are presented in Fig. 15. These cases contain the opening at the lower left-hand side corner, the one where the opening is located near the left-hand side periphery, and the last case has an opening at the left-hand side bottom corner. All the

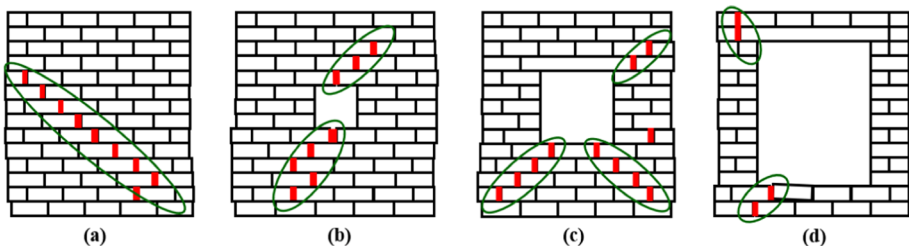


Fig. 14 Detailed cracking pattern where the maximum principal stress has been developed distribution obtained from micro modeling **a** wall with no opening, **b** wall with 25% opening, **c** wall with 50% opening, **d** wall with 75% opening

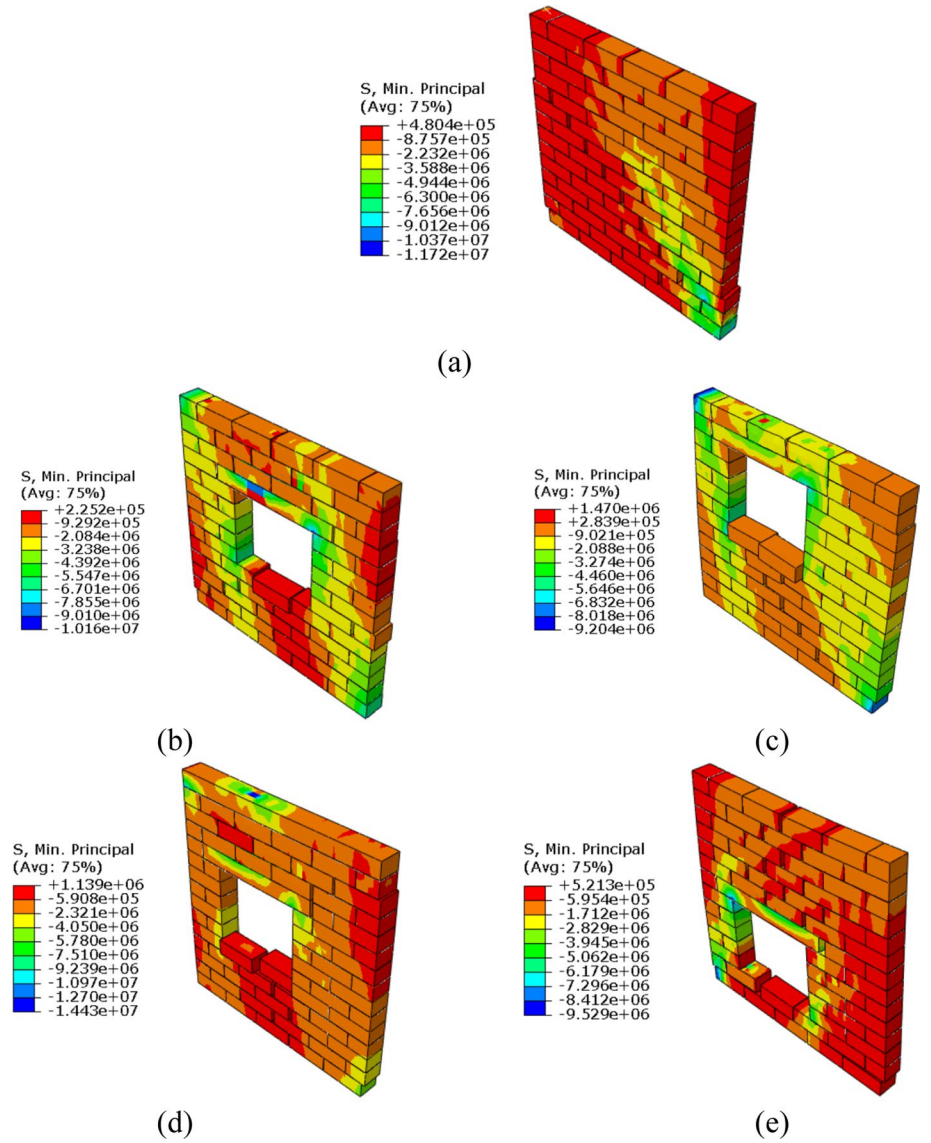


Fig. 15 Min principal stress diagram of the masonry walls with 50% opening undergoing in-plane cyclic loading, **a** without opening, **b** opening at the centre, **c** opening at the upper corner, **d** opening at the middle side, **e** opening at the bottom corner

cases are analyzed, and the results are presented to develop an understanding of how much the location of the opening may cause stress development and hysteretic energy dissipation relative to the two reference cases mentioned above.

As expected, the strength and the hysteretic energy dissipation capacity are maximum in the wall without an opening, and with the opening at the centre, the strength slightly decreases with the decrease in energy dissipation through the hysteretic curve is very low.

Due to the opening at the top, there is a 20% reduction in the maximum force-carrying capacity, and hysteretic energy dissipation is also reduced compared to the wall without an opening. While the other three cases, as given in Fig. 15c–e, a gradual reduction in the maximum load-carrying capacity are observed. Hysteretic energy in all three cases is reduced as compared to the one exhibited by the wall with no opening. However, the most interesting point is that all the cases with an opening almost show the same hysteretic energy dissipation capacity, and thus, it may appear that the location of the opening doesn't influence the hysteretic behaviour, though, as mentioned earlier, it causes a small drop in maximum force carrying capacity as observed from the hysteresis curves presented in Fig. 16 for the cases represented by Fig. 15c, d, e respectively. The wall becomes tremendously vulnerable if the corner opening lies near the bottom-most corner load is being applied. This may be due to the increased surcharge dead loads from the bricks set above. In fact, looking at the overall scenario, it may be described that if the opening is unavoidable for a functional reason, it should be placed in the central region of the masonry wall as far as the practical reason.

4.4 Effect of cyclic loading applied on the strengthened masonry walls

Cost-effective strengthening measures are essential for masonry structures to sustain lateral earthquake loadings. Therefore, an effort has been made to improve the performance of the URM walls with the use of cost-effective strengthening materials like Polypropylene bands and wire meshes, as shown in Fig. 17. The properties of the strengthening materials are considered from the test data available in the previous literature which were tested experimentally (Nayak and Dutta 2016b, a; Banerjee et al. 2019). The effect on the performance of the URM walls with different opening percentages is shown in the following subsections.

4.4.1 Improvement in performance of the masonry walls strengthened with wire meshes

The first strengthening method to be studied here is the application of wire mesh. As recommended, the steel meshes are most effective in the relatively weaker regions, i.e., the corner and joints at the bottom and top of the walls (Gambarotta and Lagomarsino 1997). However, here the wire meshes are used throughout the wall. The steel wire mesh is 1 mm

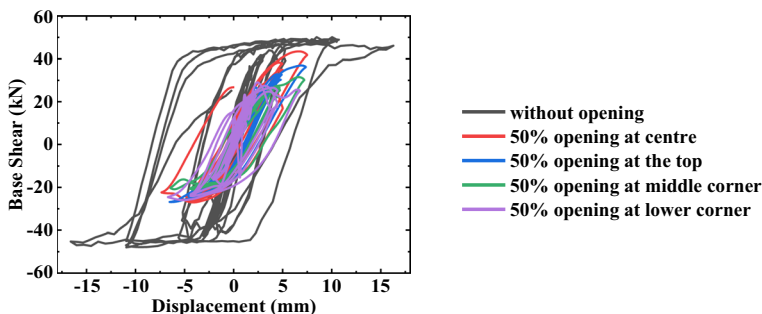


Fig. 16 Load–displacement curve for the masonry walls under cyclic loading

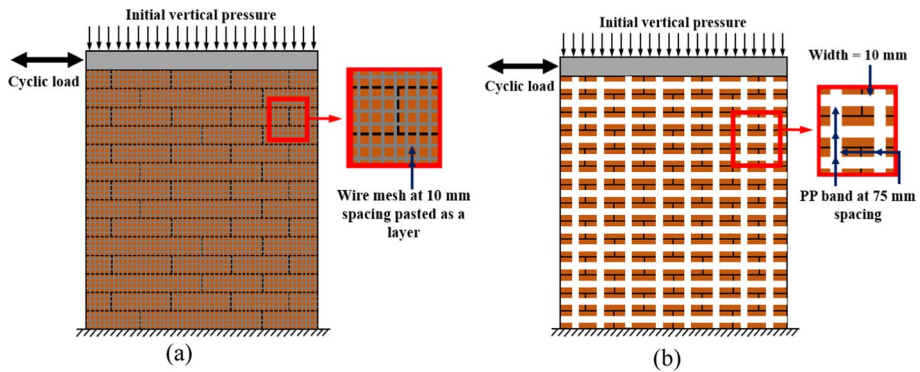


Fig. 17 Strengthening measures **a** Strengthened URM walls with wire mesh, **b** Strengthened URM walls with PP bands

in diameter with 5 mm spacing in both directions (Gambarotta and Lagomarsino 1997). In practice, the steel wire mesh is rendered with a layer of cement mortar just to protect the steel wire mesh. Therefore, in the model, a uniform 10 mm layer of cement mortar is planned to be applied, and on top of this, the steel wire mesh is supposed to be placed and modelled accordingly. The details of the reinforcement geometry are shown in Fig. 16a.

The walls were simulated using the similar cyclic loading discussed in Sect. 4.2. The minimum stress distribution for the composite walls and the individual stress distribution for both the walls and wire meshes are shown in Fig. 18. The first column is for the composite wall. The second column is shown for the wall alone, and the last column is for wire mesh alone for better understanding. It can be observed that the composite walls are carrying more stress if it is compared with the walls in Fig. 12. However, the wire meshes are carrying more stress, and less stress is transferring to the URM walls. Figure 20 presents the load–displacement diagram of the strengthened walls. Such hysteresis load–displacement plots containing four different cases of openings, namely, the URM wall without opening, the wall with 25% opening, the wall with 50% opening, and the wall with 75% opening, are presented for the strengthened wall with wire meshes and PP bands. In each case, the strength improvement of the strengthened URM walls strengthened with wire meshes is almost 2.0–3.21 times that of the nonstrengthened URM walls. The ductility capacity is also significantly improved in the same order. The details of the increase in percentages are shown in Table 3. It is evident from the results that the strengthening measures for the walls with more than 50% of the opening are not that much effective. So, it is better to keep the percentage of opening under 50% for the URM buildings.

4.4.2 Improvement in performance of the URM walls strengthened with PP bands

The second strengthening technique to be examined is the application of the PP bands. The PP bands are also effective in improving the performance of the URM walls, as recommended (Nayak et al. 2018; Heydariha et al. 2019). The width of the PP bands is 10 mm, and the spacing between them is 75 mm in both directions. In practice, the PP bands are used as a binder strip around the wall. Therefore, in the model, a uniform grid of 75 mm distances is modelled to paste on the URM wall. The details of the reinforcement geometry are shown in Fig. 17b.

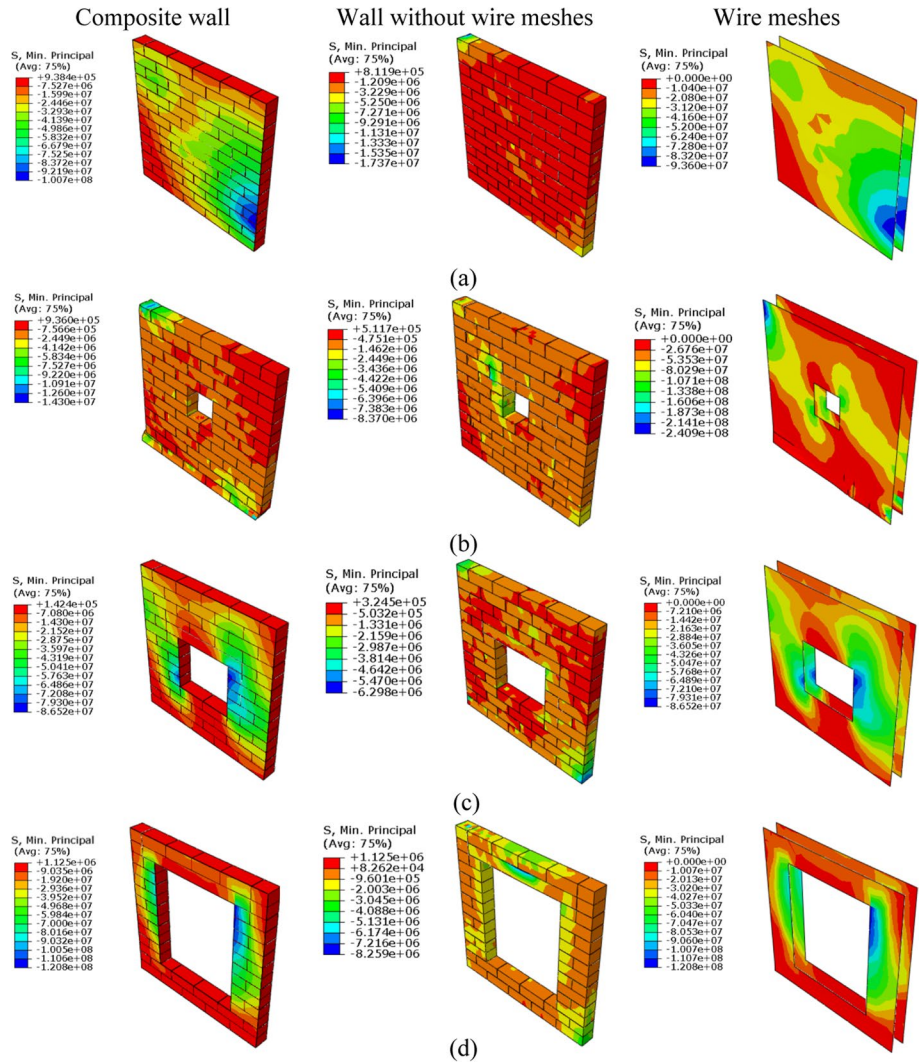


Fig. 18 Min principal stresses for the URM walls strengthened with wire meshes under static cyclic loading, **a** wall with no opening, **b** wall with 25% opening, **c** wall with 50% opening, **d** wall with 75% opening

Table 3 Increase in lateral strength of the URM walls strengthened with wire mesh

Strengthening measures type	Strength increase in percentage (%)			
	0% opening	25% opening	50% opening	75% opening
Wire meshes	321%	300%	235%	200%

The strengthened URM walls were studied using the similar cyclic loading discussed in Sect. 4.2. The minimum stress distribution for the strengthened URM walls by PP bands is shown in Fig. 19, as done for wire meshes. The first column is for the composite wall. The second column is shown for the PP bands alone, and the last column is for the URM wall alone, as done for wire meshes. Here also, PP bands carry more stress, and fewer stresses are transferred to the URM walls making the wall more resistant. As shown in Fig. 20, the strength improvement for the strengthened masonry walls with PP bands is almost 1.5–1.81 times compared to the nonstrengthened URM walls in each case. But the improvements in the ductility capacity are not that significant. The

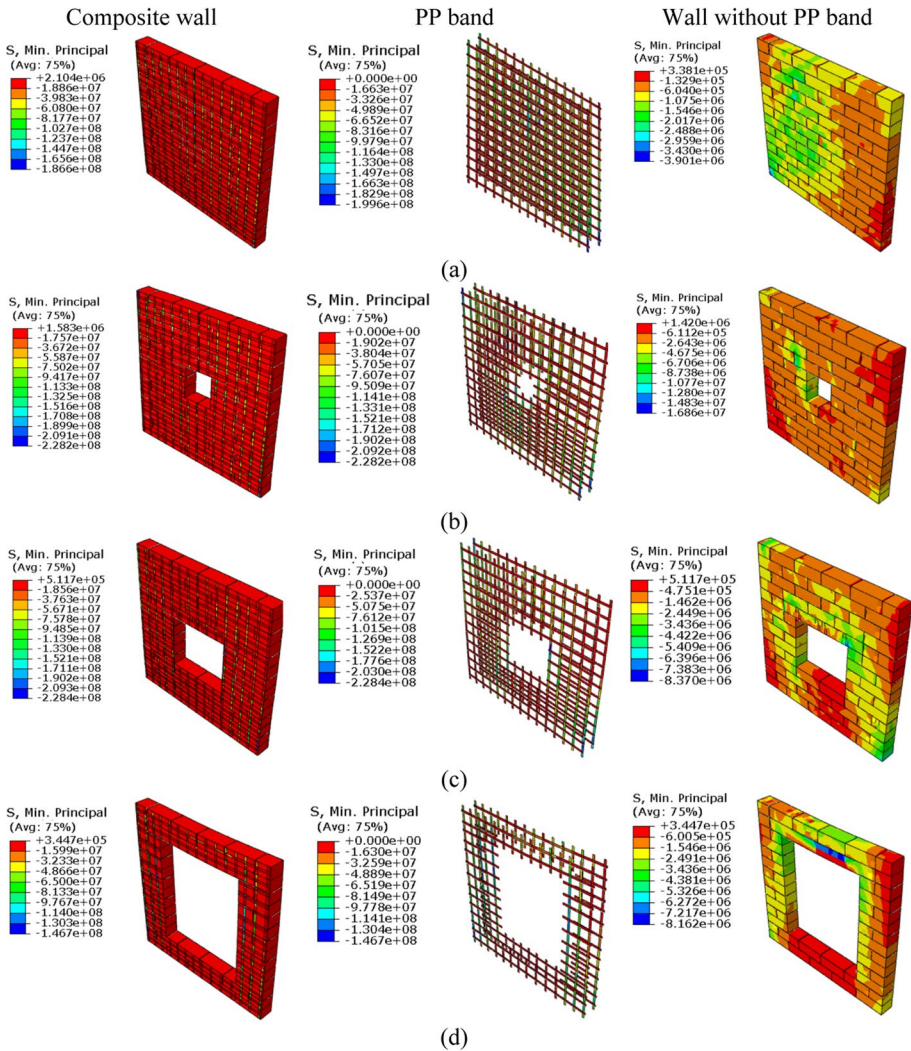


Fig. 19 Min principal stresses for the URM walls strengthened with PP bands under static cyclic loading, **a** wall with no opening, **b** wall with 25% opening, **c** wall with 50% opening, **d** wall with 75% opening

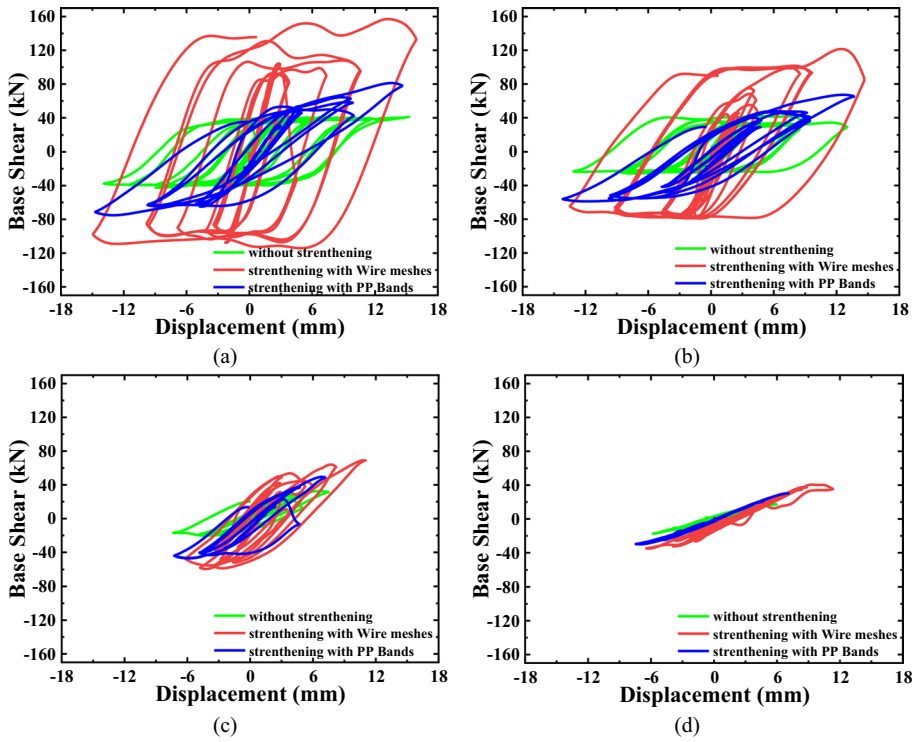


Fig. 20 Load–displacement curve for the URM walls without strengthening and strengthened with wire meshes and PP bands under in-plane cyclic loading **a** wall with no opening, **b** wall with 25% opening, **c** wall with 50% opening, **d** wall with 75% opening

Table 4 Increase in lateral strength of the URM walls strengthened with PP band

Strengthening measures type	Strength increase in percentage (%)			
	0% opening	25% opening	50% opening	75% opening
PP bands	181%	175%	157%	150%

detailed increase in percentages is shown in Table 4. Here also, the PP band strengthening for the URM walls with more than 50% of the opening is not that much effective.

On the other hand, the yield displacement also increased about 2–3 times as compared to the nonstrengthened walls with each type of opening for both PP bands and wire meshes. This clearly shows that PP band and wire mesh strengthening methods effectively sustain more lateral loads. The ductility of these walls may be expected to increase as PP band and wire meshes both are of ductile nature.

5 Conclusions

The present study attempts to address a real-life problem regarding the effect of different opening percentages and locations on the seismic performance of the URM walls. The effects of strengthening measures by PP bands and wire meshes are also studied on the same wall. This study considers an appropriate simplified FE model for studying the URM wall behaviour under in-plane lateral loading. The proposed models include surface-based cohesive behaviour to capture the elastic and plastic behaviour and a Drucker Prager (D-P) plasticity model to analyze the masonry crushing under compressive stresses. The following broad conclusions can be summarized from the present study.

- (a) The effect of opening percentages is a critical factor in the performance of URM structures during severe earthquake events. For this, a simplified FE numerical model has been used to accurately quantify the effect of the opening percentages, which is very difficult with the experimental approach. The quasi-static response of URM walls can be successfully simulated using a simplified micro-model of the URM walls. This modelling approach can accurately capture the nature of failure patterns up to and including wall collapse. This method has been very recently used in a few earlier studies (Abdulla et al. 2017; Debnath et al. 2023).
- (b) The in-plane concentrated, and cyclic loadings on the URM walls with different opening percentages are presented. Here, a drastic reduction has been noticed in the load-carrying capacity with the increase in opening percentages. For walls with a central opening, when the opening percentage is less than 25%, the wall can retain more than 80% of the capacity exhibited by the wall with no opening. When the opening percentage of the wall exceeds more than 50%, only about 20% of the residual wall capacity remains.
- (c) The position of the opening is also significant for the analysis of the URM structures. The opening position at the lower corner is the most vulnerable one, whereas the opening position at the top corner is proved to be less vulnerable. It can be predicted that the variations in the number and shape of the openings also may influence the failure mechanism in URM, drastically reducing wall strength which is already discussed in detail in the results. So, it is advised to use URM walls accounting for the residual capacity of walls containing openings. The present study can be used as a broad guiding literature for choosing the adequate extent and location of openings.
- (d) Regarding the strengthening concern, using PP band in the criss-cross pattern can improve the lateral load-carrying capacity in the range of 1.5 to 1.81. Further, the wire mesh tied on two sides of the walls also exhibits considerable improvements in the lateral load-carrying capacity, which is in the range of 2.0–3.21 times that of the reference URM wall without strengthening. The yield displacements also increased due to the strengthening of URM walls. This may reduce the effect of opening and can resist severe earthquakes due to its increased ductility.

The prime contribution of this study lies in exploring the different aspects of the effect of openings in URM walls with the help of adequate numerical modelling. The cases presented in the paper can not only give an idea about the change in behaviour due to openings for quite a few practically used specific cases but also provide a set of qualitative guidelines about the same. In this context, it is worth mentioning that because of the presence of the openings, the stress concentrations are noticed at the corner of the openings, which

may cause the propagation of cracks. However, the study not only restrict itself only to the behavioural part. Along with that, the effect of the various strengthening measures is also provided in detail, and there it has been noticed that these strengthening measures can diminish the effect of reduction in load-carrying capacity due to openings. Further, crack propagation from the corner of the openings reduces due to the use of retrofitting as it attributes tension carrying capacity.

6 Conflict of interests

The authors have no relevant financial or non-financial interests to disclose.

Acknowledgements The authors acknowledge the technical input given by Prof. Lee Cunningham, Department of Mechanical, Aerospace & Civil Engineering of the University of Manchester, UK., and Prof. Abdul Hamid Sheikh of the School of Civil, Environmental and Mining Engineering of The University of Adelaide to have this paper into its present shape.

Authors contributions PD: Methodology, Investigation, Visualization, Writing—original draft. SCD: Conceptualization, Methodology, Writing—original draft, Review and Editing, Supervision. LH: Review and Editing. BC: Review and Editing.

Data availability The data sets used or analyzed in this study are available from the corresponding author upon reasonable request.

Code availability No code was developed in the frame of this study.

References

- Abaqus (2022) ABAQUS online documentation. SIMULIA Inc
- Abasi A, Hassanli R, Vincent T, Manalo A (2020) Influence of prism geometry on the compressive strength of concrete masonry. *Constr Build Mater* 264:1. <https://doi.org/10.1016/j.conbuildmat.2020.120182>
- Abdulla KF, Cunningham LS, Gillie M (2018) Effectiveness of Strengthening Approaches for Existing Earthen Construction. In: The University of Manchester Research
- Abdulla KF, Cunningham LS, Gillie M (2017) Simulating masonry wall behaviour using a simplified micro-model approach. *Eng Struct* 151:349–365. <https://doi.org/10.1016/j.engstruct.2017.08.021>
- ACI (2013) Guide to design and construction of externally bonded fabric-reinforced cementitious matrix (FRCM) systems for repair and strengthening concrete and masonry structures
- Akhoundi F, Vasconcelos G, Lourenço P et al (2018) In-plane behavior of cavity masonry infills and strengthening with textile reinforced mortar. *Eng Struct* 156:145–160. <https://doi.org/10.1016/j.engstruct.2017.11.002>
- Alfano G, Sacco E (2006) Combining interface damage and friction in a cohesive-zone model. *Int J Numer Methods Eng* 68:542–582. <https://doi.org/10.1002/nme.1728>
- Babaeidarabad S, De Caso F, Nanni A (2014) URM Walls strengthened with fabric-reinforced cementitious matrix composite subjected to diagonal compression. *J Compos Constr* 18:04013045. [https://doi.org/10.1061/\(asce\)cc.1943-5614.0000441](https://doi.org/10.1061/(asce)cc.1943-5614.0000441)
- Banerjee S, Nayak S, Das S (2019) Enhancing the flexural behaviour of masonry wallet using PP band and steel wire mesh. *Constr Build Mater* 194:179–191. <https://doi.org/10.1016/j.conbuildmat.2018.11.001>
- Baraldi D, Cecchi A (2018) Discrete and continuous models for static and modal analysis of out of plane loaded masonry. *Comput Struct* 207:171–186. <https://doi.org/10.1016/j.compstruc.2017.03.015>
- Barenblatt GI (1962) The mathematical theory of equilibrium cracks in brittle fracture. *Adv Appl Mech* 7:55–129
- Beatini V, Royer-Carfagni G, Tasora A (2017) A regularized non-smooth contact dynamics approach for architectural masonry structures. *Comput Struct* 187:88–100. <https://doi.org/10.1016/j.compstruc.2017.02.002>

- Belytschko T, Black T (1999) Elastic crack growth in finite elements with minimal remeshing. *Int J Numer Meth Eng* 45:601–620
- Benzeggagh ML, Kenane M (1996) Measurement of mixed-mode delamination fracture toughness of unidirectional glass/epoxy composites with mixed-mode bending apparatus. *Compos Sci Technol* 56:439–449
- Bhattacharya S, Nayak S, Dutta SC (2014) A critical review of retrofitting methods for unreinforced masonry structures. *Int J Disast Risk Reduct* 7:51–67. <https://doi.org/10.1016/j.ijdr.2013.12.004>
- Bolhassani M, Hamid A, Moon F, Professor A (2016) Enhancement of lateral in-plane capacity of partially grouted concrete masonry shear walls. *Eng Struct* 108:59–76
- Bolhassani M, Hamid AA, Lau ACW, Moon F (2015) Simplified micro modeling of partially grouted masonry assemblages. *Constr Build Mater* 83:159–173. <https://doi.org/10.1016/j.conbuildmat.2015.03.021>
- Brasile S, Casciaro R, Formica G (2010) Finite Element formulation for nonlinear analysis of masonry walls. *Comput Struct* 88:135–143. <https://doi.org/10.1016/j.compstruc.2009.08.006>
- Bui TT, Limam A, Sarhosis V, Hjjaj M (2017) Discrete element modelling of the in-plane and out-of-plane behaviour of dry-joint masonry wall constructions. *Eng Struct* 136:277–294. <https://doi.org/10.1016/j.engstruct.2017.01.020>
- Camanho PP, Dávila CG (2002) Mixed-mode decohesion finite elements for the simulation of delamination in composite materials
- Campilho R, de Moura M, Domingues J (2008) Using a cohesive damage model to predict the tensile behaviour of CFRP single-strap repairs. *Int J Solids Struct* 45:1497–1512. <https://doi.org/10.1016/j.ijsolstr.2007.10.003>
- Casacci S, Gentilini C, Tommaso AD, Oliveira DV (2019) Shear strengthening of masonry wallettes resorting to structural repointing and FRCM composites. *Constr Build Mater* 206:19–34. <https://doi.org/10.1016/j.conbuildmat.2019.02.044>
- Casolo S (2004) Modelling in-plane micro-structure of masonry walls by rigid elements. *Int J Solids Struct* 41:3625–3641. <https://doi.org/10.1016/j.ijsolstr.2004.02.002>
- Chourasia A, Singhal S, Parashar J (2019) Experimental investigation of seismic strengthening technique for confined masonry buildings. *J Build Eng* 25:1. <https://doi.org/10.1016/j.jobe.2019.100834>
- D’Altri AM, de Miranda S, Castellazzi G, Sarhosis V (2018) A 3D detailed micro-model for the in-plane and out-of-plane numerical analysis of masonry panels. *Comput Struct* 206:18–30. <https://doi.org/10.1016/j.compstruc.2018.06.007>
- D’Altri AM, Sarhosis V, Milani G et al (2020) Modeling strategies for the computational analysis of unreinforced masonry structures: review and classification. *Arch Comput Methods Eng* 27:1153–1185. <https://doi.org/10.1007/s11831-019-09351-x>
- Deb T, Yuen TYP, Lee D et al (2021) Bi-directional collapse fragility assessment by DFEM of unreinforced masonry buildings with openings and different confinement configurations. *Earthq Eng Struct Dyn* 50:4097–4120. <https://doi.org/10.1002/eqe.3547>
- Debnath P, Dutta SC, Mandal P (2023) Lateral behaviour of masonry walls with different types of brick bonds, aspect ratio and strengthening measures by polypropylene bands and wire mesh. *Structures* 49:623–639. <https://doi.org/10.1016/j.istruc.2023.01.155>
- Drucker DC, Prager W (1952) Soil mechanics and plastic analysis or limit design. *Q Appl Math* 10(2):157–165
- Dugdale DS (1960) Yielding of steel sheets containing slits. *J Me& Phys Solids* 8:100–104
- Formica G, Sansalone V, Casciaro R (2002) A mixed solution strategy for the nonlinear analysis of brick masonry walls. *Comput Methods Appl Mech Engrg* 191:5847–5876
- Fouchal F, Lebon F, Titeux I (2009) Contribution to the modelling of interfaces in masonry construction. *Constr Build Mater* 23:2428–2441. <https://doi.org/10.1016/j.conbuildmat.2008.10.011>
- Gambarotta L, Lagomarsino S (1997) Damage models for the seismic response of brick masonry shear walls. Part I: the mortar joint model and its applications. *Earthq Eng Struct Dyn* 26:423–439
- Giaretton M, Dizhur D, Garbin E et al (2018) In-Plane Strengthening of Clay Brick and Block Masonry Walls Using Textile-Reinforced Mortar. *J Compos Constr* 22:04018028. [https://doi.org/10.1061/\(asce\)cc.1943-5614.0000866](https://doi.org/10.1061/(asce)cc.1943-5614.0000866)
- Hendry AW (1998) *Structural masonry*. Palgrave MacMillan, UK
- Heydariha JZ, Ghaednia H, Nayak S et al (2019) Experimental and Field Performance of PP Band-Retrofitted Masonry: Evaluation of Seismic Behavior. *J Perform Constr Facil* 33:04018086. [https://doi.org/10.1061/\(asce\)cf.1943-5509.0001233](https://doi.org/10.1061/(asce)cf.1943-5509.0001233)
- IS 456 (2000) *Plain and Reinforced Concrete - Code of Practice*. New Delhi
- IS 2250 (1981) *Code of Practice for Preparation and Use of Masonry Mortars*. New Delhi

- Ismail N, Ingham JM (2016) In-plane and out-of-plane testing of unreinforced masonry walls strengthened using polymer textile reinforced mortar. *Eng Struct* 118:167–177. <https://doi.org/10.1016/j.engstruct.2016.03.041>
- Khattak N, Derakhshan H, Thambiratnam D, et al (2021) Applied Element Modelling of the Out-of-Plane Bending Behaviour of Single Leaf Unreinforced Masonry Walls. In: Australian Earthquake Engineering Society
- Lemos JV (2007) Discrete element modeling of masonry structures. *Int J Architect Herit* 1:190–213. <https://doi.org/10.1080/15583050601176868>
- Lourenço PB (2002) Computations on historic masonry structures. *Prog Struct Mat Eng* 4:301–319. <https://doi.org/10.1002/pse.120>
- Lourenço PB (1996) Computational strategies for masonry structures. Delft University of Technology, TU Delft
- Lourenço PB, Rots JG (1997) Multisurface interface model for analysis of masonry structures cap model for masonry. *J Eng Mech* 123:660–668
- Macabuag J, Guragain R, Bhattacharya S (2012) Seismic retrofitting of non-engineered masonry in rural Nepal. *Proc Inst Civ Eng Struct Build* 165:273–286. <https://doi.org/10.1680/stbu.10.00015>
- Macorini L, Izzuddin BA (2011) A non-linear interface element for 3D mesoscale analysis of brick-masonry structures. *Int J Numer Methods Eng* 85:1584–1608. <https://doi.org/10.1002/nme.3046>
- Melenk JM, Babuška I (1996) The partition of unity finite element method: Basic theory and applications. *Comput Methods Appl Mech Engrg* 139:289–314
- Moes N, Dolbow J, Belytschko T (1999) A finite element method for crack growth without remeshing. *Int J Numer Methods Eng* 46:131–150
- Mojsilović N, Page A (2009) Static-cyclic shear tests on masonry wallettes with a damp-proof course membrane
- Naciri K, Aalil I, Chaaba A, Al-Mukhtar M (2021a) Detailed micromodeling and multiscale modeling of masonry under confined shear and compressive loading. *Pract Period Struct Des Constr* 26:04020056. [https://doi.org/10.1061/\(asce\)sc.1943-5576.0000538](https://doi.org/10.1061/(asce)sc.1943-5576.0000538)
- Naciri K, Aalil I, Chaaba A, Al-Mukhtar M (2021b) Detailed micromodeling and multiscale modeling of masonry under confined shear and compressive loading. *Pract Period Struct Des Constr* 26:1. [https://doi.org/10.1061/\(asce\)sc.1943-5576.0000538](https://doi.org/10.1061/(asce)sc.1943-5576.0000538)
- Nayak S, Banerjee S, Das S (2018) Augmenting out-of-plane behaviour of masonry wallet using PP-band and steel wire mesh. In: IOP Conference Series: Materials Science and Engineering. Institute of Physics Publishing
- Nayak S, Dutta SC (2016a) Improving seismic performance of masonry structures with openings by polypropylene bands and L-shaped reinforcing bars. *J Perform Constr Facil* 30:04015003. [https://doi.org/10.1061/\(asce\)cf.1943-5509.0000733](https://doi.org/10.1061/(asce)cf.1943-5509.0000733)
- Nayak S, Dutta SC (2016b) Failure of masonry structures in earthquake: a few simple cost effective techniques as possible solutions. *Eng Struct* 106:53–67. <https://doi.org/10.1016/j.engstruct.2015.10.014>
- Parrinello F, Failla B, Borino G (2009) Cohesive-frictional interface constitutive model. *Int J Solids Struct* 46:2680–2692. <https://doi.org/10.1016/j.ijsolstr.2009.02.016>
- Pegon P, Anthoine A (1997) Numerical Strategies for solving continuum damage problems with softening: application to the homogenization of masonry. *Comput Struct* 64:623–642
- Petracca M, Pelà L, Rossi R et al (2017) Micro-scale continuous and discrete numerical models for nonlinear analysis of masonry shear walls. *Constr Build Mater* 149:296–314. <https://doi.org/10.1016/j.conbuilmat.2017.05.130>
- Pluijm R van der (1992) Material properties of masonry and its components under tension and shear. In: 6th Canadian Masonry Symposium. Saskatoon, Canada
- Sagar SL, Singhal V, Rai DC, Gudur P (2017) Diagonal shear and out-of-plane flexural strength of fabric-reinforced cementitious matrix-strengthened masonry wallettes. *J Compos Constr* 21:04017016. [https://doi.org/10.1061/\(asce\)cc.1943-5614.0000796](https://doi.org/10.1061/(asce)cc.1943-5614.0000796)
- Salsavilca J, Tarque N, Yacila J, Camata G (2020) Numerical analysis of bonding between masonry and steel reinforced grout using a plastic–damage model for lime–based mortar. *Constr Build Mater* 262:1. <https://doi.org/10.1016/j.conbuilmat.2020.120373>
- Schildkamp M, Silvestri S, Araki Y (2020) Rubble stone masonry buildings with cement mortar: design specifications in seismic and masonry codes worldwide. *Front Built Environ* 6:1
- Shabdin M, Zargaran M, Attari NKA (2018) Experimental diagonal tension (shear) test of Un-Reinforced Masonry (URM) walls strengthened with textile reinforced mortar (TRM). *Constr Build Mater* 164:704–715. <https://doi.org/10.1016/j.conbuilmat.2017.12.234>
- Smoljanović H, Nikolić Ž, Živaljić N (2015) A combined finite-discrete numerical model for analysis of masonry structures. *Eng Fract Mech* 136:1–14. <https://doi.org/10.1016/j.engfracmech.2015.02.006>

- Stefanou I, Sab K, Heck J-V (2014) Three dimensional homogenization of masonry structures with building blocks of finite strength: A closed form strength domain. *J Solids Struct*. <https://doi.org/10.1016/j.jssolstr.2014.10.007>
- Thakur A, Senthil K, Singh AP, Iqbal MA (2020) Prediction of dynamic amplification factor on clay brick masonry assemblage. *Structures* 27:673–686. <https://doi.org/10.1016/j.istruc.2020.06.009>
- Toti J, Gattulli V, Sacco E (2015) Nonlocal damage propagation in the dynamics of masonry elements. *Comput Struct* 152:215–227. <https://doi.org/10.1016/j.compstruc.2015.01.011>
- Vasconcelos G, Lourenço PB (2009) In-Plane Experimental Behavior of Stone Masonry Walls under Cyclic Loading. *J Struct Eng* 135:1269–1277. <https://doi.org/10.1061/ASCEST.1943-541X.0000053>
- Wilding BV, Godio M, Beyer K (2020) The ratio of shear to elastic modulus of in-plane loaded masonry. *Mater Struct/materiaux Et Constructions* 53:1. <https://doi.org/10.1617/s11527-020-01464-1>
- Yardim Y, Lalaj O (2016) Shear strengthening of unreinforced masonry wall with different fiber reinforced mortar jacketing. *Constr Build Mater* 102:149–154. <https://doi.org/10.1016/j.conbuildmat.2015.10.095>
- Zhang S, Yang D, Sheng Y et al (2017) Numerical modelling of FRP-reinforced masonry walls under in-plane seismic loading. *Constr Build Mater* 134:649–663. <https://doi.org/10.1016/j.conbuildmat.2016.12.091>
- Zhang Y, Wang Z, Jiang L et al (2022) Seismic analysis method of unreinforced masonry structures subjected to mainshock-aftershock sequences. *Bull Earthq Eng* 20:2619–2641. <https://doi.org/10.1007/S10518-022-01334-X/FIGURES/11>

Publisher's Note Springer Nature remains neutral with regard to jurisdictional claims in published maps and institutional affiliations.

Springer Nature or its licensor (e.g. a society or other partner) holds exclusive rights to this article under a publishing agreement with the author(s) or other rightsholder(s); author self-archiving of the accepted manuscript version of this article is solely governed by the terms of such publishing agreement and applicable law.

Authors and Affiliations

Pranoy Debnath¹ · Sekhar Chandra Dutta¹ · Lipika Halder² · Bishwajeet Choubey³

✉ Sekhar Chandra Dutta
sekhar@iitism.ac.in

Pranoy Debnath
pranoydebnath.20dr0099@cve.iitism.ac.in; pranoy.debnath9@gmail.com

Lipika Halder
erlhalder@yahoo.co.in

Bishwajeet Choubey
bishwajeetchoubey@gmail.com

¹ Department of Civil Engineering, Indian Institute of Technology (ISM) Dhanbad, Dhanbad, Jharkhand 826004, India

² Department of Civil Engineering, National Institute of Technology Agartala, Tripura 799046, India

³ Chief Construction Engineer (R&D), DRDO South, Hyderabad, Telangana 500003, India